Stability and Decay Rates of Non-Isotropic Attractive Bose-Einstein Condensates

C. Huepe[1,4], L.S. Tuckerman[2], S. Métens[3,4], and M. E. Brachet[4]

[1] *Department of Engineering Sciences and Applied Mathematics,*
Northwestern University, 2145 Sheridan Road, Evanston, IL 60208, USA
[2] *Laboratoire d'Informatique pour la Mécanique et les Sciences de l'Ingénieur, BP 133, 91403 Orsay, France*
[3] *Laboratoire de Physique Théorique de la Matière Condensée, Université Paris VII, Paris, France*
[4] *Laboratoire de Physique Statistique de l'Ecole Normale Supérieure,*
associé au CNRS et aux Universités Paris VI et VII, 24 Rue Lhomond, 75231 Paris, France

(Dated: February 1, 2008)

Non-Isotropic Attractive Bose-Einstein condensates are investigated with Newton and inverse Arnoldi methods. The stationary solutions of the Gross-Pitaevskii equation and their linear stability are computed. Bifurcation diagrams are calculated and used to find the condensate decay rates corresponding to macroscopic quantum tunneling, two-three body inelastic collisions and thermally induced collapse.

Isotropic and non-isotropic condensates are compared. The effect of anisotropy on the bifurcation diagram and the decay rates is discussed. Spontaneous isotropization of the condensates is found to occur. The influence of isotropization on the decay rates is characterized near the critical point.

Contents

I. INTRODUCTION

Experimental Bose-Einstein condensation (BEC) with attractive interactions was first realized in ultra cold vapors of ^{7}Li atoms [1], opening a new field in the study of macroscopic quantum phenomena. Such attractive condensates are known to be metastable in spatially localized systems, provided that the number of condensed particles is below a critical value $\mathcal{N}_c$ [2]. More recently, Feshbach resonances in BEC of ^{85}Rb atoms were used to investigate the stability and dynamics of condensates with two-body interactions going from repulsive to attractive values [3].

Experimental atomic traps generally use a harmonic and slightly asymmetric potential. Thus, for most of the condensates produced so far, the geometry is nearly spherical. However, extremely asymmetric traps have been recently employed in experimental investigations of cigar-like [4, 5, 6] or pancake-like [7] condensates.

Various physical processes compete to determine the lifetime of attractive condensates. The processes considered in this paper are macroscopic quantum tunneling (MQT) [8, 9], inelastic two and three body collisions (ICO) [10, 11, 12] and thermally induced collapse (TIC) [9, 13]. The MQT and TIC contributions have been evaluated in the literature using a variational Gaussian approximation to the condensate wave function. However, this approximation is known to be in substantial quantitative error – e.g. as high as 17% for $\mathcal{N}_c$ [8, 14, 15] – when compared to the exact solution of the Gross-Pitaevskii (G-P) equation.

In the nearly spherical isotropic case, both the elliptic (stable) and the hyperbolic (unstable) exact stationary solutions of the G-P equation were obtained numerically by Newton's method in [15]. These solution branches were shown to meet at $\mathcal{N}_c$ through a generic Hamiltonian Saddle Node (HSN) bifurcation. While the Gaussian approximation presents an analogous HSN bifurcation, the amplitudes of its associated scaling laws were found to be in substantial ($\geq 14\%$) error. A method for computing the unstable branch in the isotropic case via a shooting method was outlined in [16], but generalizing this procedure to higher dimensions would be inefficient, and impossible in non-rectangular domains. The decay rates for the processes of MQT, ICO and TIC were also

computed, in the spherical case, from the numerical G-P solutions. They were shown to obey universal scaling laws. Experimentally significant quantitative differences were found between the exact rates and those based on the Gaussian approximation [15].

In the extreme anisotropic cases, the variational Gaussian approximation has been computed and compared to the G-P solution on the elliptic (stable) branch [17, 18]. This has allowed a more reliable determination of the critical value $\mathcal{N}_c$ than can be obtained by the Gaussian approximation [17]. However, a faithful determination of the lifetimes needs the computation of the hyperbolic (unstable) branch [15], which has not yet been performed in the anisotropic case.

The main purpose of the present paper is to show that it is possible to compute the full HSN bifurcation diagram, and the corresponding lifetimes, in extreme anisotropic cases. We will do so by studying a cigar-like and a pancake-like condensate, and will obtain their MQT, ICO and TIC decay rates. While we have concentrated, for simplicity, on these two axisymmetric cases, the new numerical methods developed in this work are capable of solving the general anisotropic problem.

The paper is organized as follows. In section II we present the model considered throughout this work. After defining our working form of the G-P equation, we explain the methods that we used to obtain the stationary states and their linearized stability. Section III is devoted to the numerical determination of the bifurcation diagram and stability of the stationary states. Isotropic and non-isotropic cases are compared and the dynamics is discussed in terms of the HSN bifurcation. In section IV we define and compute the decay rates. Isotropic and non-isotropic rates are discussed, their similarity is analyzed in terms of the spontaneous isotropization of condensates. Finally, section V is our conclusion. Details of our numerical methods are given in the Appendix.

II. PRESENTATION OF THE MODEL

A. Gross-Pitaevskii Equation

At low enough temperatures, neglecting the thermal and quantum fluctuations, a Bose condensate can be represented by a complex wave function $\Psi(\mathbf{x}, t)$ that obeys the dynamics of the G-P equation [19, 20]. Specifically, we consider a condensate of $\mathcal{N}$ particles of mass m and (negative) effective scattering length $\tilde{a}$ in a confining harmonic potential $V(\tilde{\mathbf{x}}) = m(\tilde{\omega}_x^2\tilde{x}^2 + \tilde{\omega}_y^2\tilde{y}^2 + \tilde{\omega}_z^2\tilde{z}^2)/2$ where $\tilde{\mathbf{x}} = (\tilde{x}, \tilde{y}, \tilde{z})$ is the position vector.

These variables can be rescaled with respect to any reference frequency $\hat{\omega}$ by using the natural quantum harmonic oscillator units of time $\tau_0 = 1/\hat{\omega}$ and length $L_0 = \sqrt{\hbar/m\hat{\omega}}$. In terms of the non-dimensional variables $t = \tilde{t}/\tau_0$, $\mathbf{x} = \tilde{\mathbf{x}}/L_0$, $a = 4\pi\tilde{a}/L_0$, $\omega_x = \tilde{\omega}_x/\hat{\omega}$, $\omega_y = \tilde{\omega}_y/\hat{\omega}$ and $\omega_z = \tilde{\omega}_z/\hat{\omega}$, the condensate is described

by the action

$$\mathcal{A} = \int dt \left\{ \int d^3x \frac{i}{2} \left(\bar{\Psi}\frac{\partial\Psi}{\partial t} - \Psi\frac{\partial\bar{\Psi}}{\partial t} \right) - \mathcal{F} \right\}, \quad (1)$$

with

$$\mathcal{F} = \mathcal{E} - \mu\mathcal{N} \quad (2)$$

where

$$\mathcal{N} = \int d^3x |\Psi|^2 \quad (3)$$

$$\mathcal{E} = \int d^3x \left[\frac{1}{2}|\nabla\Psi|^2 + V(\mathbf{x})|\Psi|^2 + \frac{a}{2}|\Psi|^4 \right] \quad (4)$$

$$V(\mathbf{x}) = \frac{1}{2}(\omega_x^2 x^2 + \omega_y^2 y^2 + \omega_z^2 z^2) \quad (5)$$

The Euler-Lagrange equation corresponding to $\mathcal{A}$ is our working form of the Gross-Pitaevskii equation:

$$-i\frac{\partial\Psi}{\partial t} = -\frac{\delta\mathcal{F}}{\delta\bar{\Psi}} \quad (6)$$

$$= \left[\frac{1}{2}\nabla^2 - V(\mathbf{x}) - (a|\Psi|^2 - \mu) \right] \Psi.$$

Our goal is to numerically determine the stable and unstable stationary states of (6) and the eigenvalues of (6) linearized about these stationary states. We will carry out this calculation for various values of a cylindrical potential defined by $\omega_r \equiv \omega_x = \omega_y$ and ω_z: the isotropic case $\omega_r = \omega_z$, a cigar case $\omega_r/5 = \omega_z$ and a pancake case $\omega_r = \omega_z/5$. We will then use these results to calculate the condensate decay rates and compare these decay rates to those produced by the Gaussian approximation.

B. Stationary States

Stationary states of (6) corresponding to minima of $\mathcal{E}$ at a given value of $\mathcal{N}$ can be obtained by integrating to relaxation the diffusion equation

$$\frac{\partial\Psi}{\partial t} = -\frac{\delta\mathcal{F}}{\delta\bar{\Psi}} = \left[\frac{1}{2}\nabla^2 - V(\mathbf{x}) - (a|\Psi|^2 - \mu) \right] \Psi \quad (7)$$

$$\frac{\partial\mathcal{N}}{\partial t} = 0, \quad (8)$$

using initial data $\Psi(t = 0)$ with a total number of particles $\mathcal{N}$. The condition (8) fixes the value of the Lagrange multiplier μ during the relaxation. This relaxation method yields both the solution Ψ and the Lagrange multiplier μ. It is equivalent to that used in [14] and can only reach the stable stationary solutions of (7). Unstable stationary solutions to (6) and (7) are obtained by a Newton branch following method detailed in the Appendix.

Note that the Lagrange multiplier μ can only affect the solutions of (6) through a homogeneous rotating phase factor $e^{i\mu t}$, in contrast to its particle number conservation effect on equation (7). However, every stationary solution to (6) is indexed by the unique μ-value that makes it time-independent, as shown in figure 1.
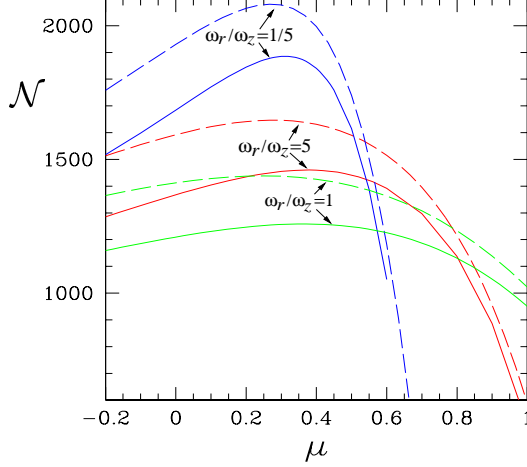
FIG. 1: Particle number $\mathcal{N}$ as a function of μ for the exact solutions (solid curves) and the Gaussian approximation (dashed curves) presented in section III. From top to bottom: pancake ($\omega_r = \omega_z/5$), cigar ($\omega_r/5 = \omega_z$), and isotropic ($\omega_r = \omega_z$) geometries.

C. Linearized Stability

We now turn our attention to computing the linear stability of the G-P equation about a stationary state. We first write (6) in the abbreviated form:

$$-i\frac{\partial \Psi}{\partial t} = L\Psi + W(\Psi) \tag{9}$$

where

$$L\Psi \equiv \frac{1}{2}\nabla^2\Psi \tag{10}$$

$$W(\Psi) \equiv \left[-V(\mathbf{x}) - a|\Psi|^2 + \mu\right]\Psi \tag{11}$$

The stationary states of (9) satisfy:

$$0 = L\Psi + W(\Psi) \tag{12}$$

Without loss of generality, Ψ can be chosen to be real. Our objective is to calculate the eigenpairs (λ, ψ) of the operator that results from linearizing (9) about a stationary state Ψ. (We use Ψ to designate solutions to the nonlinear problem (12) and ψ to designate eigenvectors, which are solutions to the linear problem to be defined below.) In order to correctly formulate the linear stability problem, it is necessary to first decompose $\psi = \psi^R + i\psi^I$. We write the linearized evolution equation

$$\frac{\partial \psi}{\partial t} = i(L + DW(\Psi))(\psi^R + i\psi^I) \tag{13}$$

where $DW(\Psi)$ is the Fréchet derivative, or Jacobian, of W evaluated at Ψ. $DW(\Psi)$ acts on ψ via:

$$DW\psi = DW^R\psi^R + iDW^I\psi^I \tag{14}$$

where we have omitted the functional dependence of DW, DW^R, and DW^I on Ψ, and where

$$DW^R \equiv \mu - V(\mathbf{x}) - 3a\Psi^2 \tag{15a}$$

$$DW^I \equiv \mu - V(\mathbf{x}) - a\Psi^2. \tag{15b}$$

Equation (13) is then written in matrix form as

$$\frac{\partial}{\partial t}\begin{pmatrix} \psi^R \\ \psi^I \end{pmatrix} = \begin{bmatrix} 0 & -(L + DW^I) \\ L + DW^R & 0 \end{bmatrix}\begin{pmatrix} \psi^R \\ \psi^I \end{pmatrix} \tag{16}$$

The eigenmodes $(\lambda, \psi^R, \psi^I)$ satisfy

$$\lambda\begin{pmatrix} \psi^R \\ \psi^I \end{pmatrix} = \begin{bmatrix} 0 & -(L + DW^I) \\ L + DW^R & 0 \end{bmatrix}\begin{pmatrix} \psi^R \\ \psi^I \end{pmatrix} \tag{17}$$

Note that this eigensystem is usually presented in the literature (see, for example, reference [22]) in terms of the variables

$$(\omega^{\mathrm{B}}, \psi, \psi^*) \equiv (-i\lambda, \psi^R + i\psi^I, \psi^R - i\psi^I) \tag{18}$$

as the equivalent Bogoliubov–de Gennes coupled equations

$$\omega^{\mathrm{B}}\begin{pmatrix} \psi \\ \psi^* \end{pmatrix} = \begin{bmatrix} L + DW^{\mathrm{B}} & -a\Psi^2 \\ a\Psi^2 & -(L - DW^{\mathrm{B}}) \end{bmatrix}\begin{pmatrix} \psi \\ \psi^* \end{pmatrix} \tag{19}$$

where

$$DW^{\mathrm{B}} \equiv \mu - V(\mathbf{x}) - 2a\Psi^2 \tag{20}$$

In the following, we will work with matrix formulation (17) because it avoids a potential notational inconsistency of (19) arising from the fact that ψ and ψ^* are complex conjugates only when ω^{B} is imaginary.

It is more convenient to work with the square of the matrix in (17):

$$\lambda^2\begin{pmatrix} \psi^R \\ \psi^I \end{pmatrix} = \tag{21}$$

$$\begin{bmatrix} -(L + DW^I)(L + DW^R) & 0 \\ 0 & -(L + DW^R)(L + DW^I) \end{bmatrix}\begin{pmatrix} \psi^R \\ \psi^I \end{pmatrix}$$

Because (21) is block diagonal, it can be separated into the two problems:

$$\lambda^2\psi^R = -(L + DW^I)(L + DW^R)\psi^R \tag{22a}$$

$$\lambda^2\psi^I = -(L + DW^R)(L + DW^I)\psi^I \tag{22b}$$

Problems (22a) and (22b) are closely related, Since the operators L, DW^I, and DW^R are all self-adjoint under the standard Euclidean inner product, the operators in (22a) and (22b) are adjoint to each other. If ψ^R is an eigenvector of (22a) with non-zero eigenvalue λ^2, then $(L + DW^R)\psi^R$ is an eigenvector of (22b) with the same eigenvalue. (Similarly, if $(\lambda, \psi^R, \psi^I)$ is an eigenmode of (17), then $(-\lambda, \psi^R, -\psi^I)$ is also an eigenmode of (17).) Thus, we solve only (22a). The eigenvalues λ^2 of (22a)-(22b) must be either complex conjugate pairs or real. We find them to be real and (almost all) negative, perturbed

only slightly from the eigenvalues of $-L^2$. The eigenvalues λ of (17) are therefore found to be either pure imaginary or pure real, with most imaginary.

Problems (17) and (22a)-(22b) have neutral eigenmodes which reflect the physical invariances of the problem. Since $DW^I\Psi = W(\Psi)$, then the stationary state Ψ is a neutral mode of $L + DW^I$ and hence of problem (22b). This neutral mode is the phase mode of (6), since its existence is a consequence of the invariance of solutions Ψ to (12) under multiplication by any complex number on the unit circle. The corresponding eigenmode of problem (22a) is $d\Psi/d\mu$. This neutral mode can be understood as a consequence of differentiating (6) with respect to μ:

$$0 = \frac{d}{d\mu}[(L + W)\Psi] = (L + DW^R)\frac{d\Psi}{d\mu} + \Psi \qquad (23)$$

Thus,

$$-(L + DW^I)(L + DW^R)\frac{d\Psi}{d\mu} = (L + DW^I)\Psi = 0. \quad (24)$$

In terms of the original problem (17), the phase mode $(\lambda, \psi^R, \psi^I) = (0, 0, \Psi)$ is a neutral eigenvector, while (23) shows that $(\lambda, \psi^R, \psi^I) = (0, d\Psi/d\mu, 0)$ is a neutral generalized eigenvector, the two modes forming a Jordan block for (17).

In practice, we fix μ to calculate the stationary states Ψ and the eigenvalues. The operators of (22a)-(22b) depend on μ both explicitly and through Ψ. For μ above a critical value μ_c all eigenvalues λ are imaginary, i.e. Ψ is an elliptic stationary state of (9). As μ crosses μ_c, we will see that one imaginary pair fuses at zero, and becomes real, with one positive and one negative value of λ for $\mu < \mu_c$. Stationary states for $\mu < \mu_c$ are thus hyperbolic in the directions corresponding to these eigenvalues.

III. BIFURCATION AND STABILITY OF CONDENSATES

In this section we will find the stationary solutions and study the stability of isotropic ($\omega_r = \omega_z$), cigar-like ($\omega_r/5 = \omega_z$) and pancake-like ($\omega_r = \omega_z/5$) condensates. These results were obtained by solving equation (12) for the stationary states and (17) or (22a) for the corresponding bifurcating eigenvalues. The system is discretized using pseudo-spectral methods in a spherical domain for the isotropic case and in a periodic Cartesian domain for the non-isotropic cases. We use Newton's method to calculate the branches of stationary states. The bifurcating eigenvalue is found in the isotropic case by diagonalizing the matrix corresponding to (17). In the non-isotropic case, we use instead the iterative inverse Arnoldi method, which requires only actions of the operator in (22a). The BiCGSTAB variant of the conjugate gradient method is used to solve the linear systems required by both Newton's method and the inverse Arnoldi method. The numerical methods we use are described in greater detail in the Appendix.
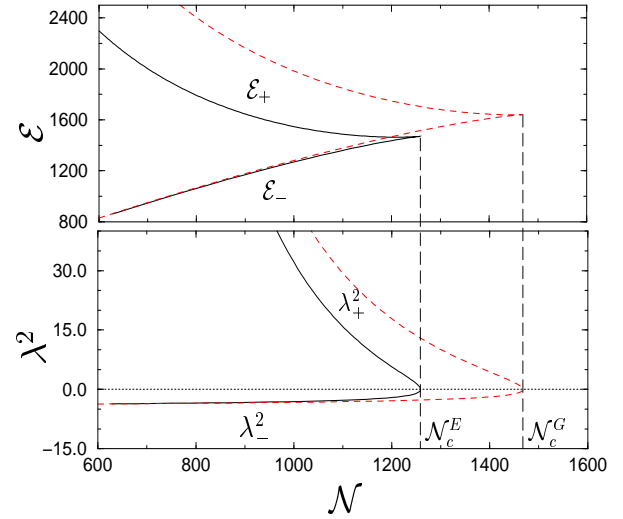

FIG. 2: Stationary solutions of the GP equation versus the particle number $\mathcal{N}$ for the isotropic potential case with $\hat{\omega}_r = \hat{\omega}_z = \hat{\omega}$. Top: value of the energy functional $\mathcal{E}_+$ on the unstable (hyperbolic) branch and $\mathcal{E}_-$ on the stable (elliptic) branch. Bottom: square of the bifurcating eigenvalue ($\lambda_\pm^2$). Note that $|\lambda_-|$ is the energy of small excitations around the stable branch. Solid lines: exact solution of the GP equation. Dashed lines: Gaussian approximation.
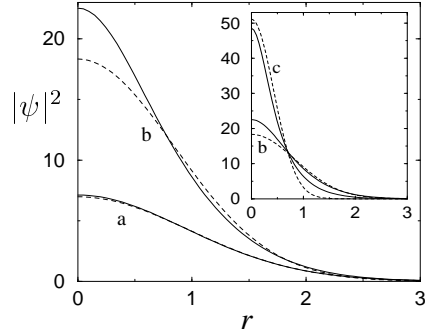

FIG. 3: Condensate density $|\psi|^2$ as a function of radius r, in reduced units (see text). Solid lines: exact solution of the G-P equation. Dashed lines: Gaussian approximation. Stable (elliptic) solutions are shown for particle number $\mathcal{N} = 252$ (a) and $\mathcal{N} = 1132$ (b). (c) is the unstable (hyperbolic) solution for $\mathcal{N} = 1132$ (see insert).

A. Isotropic Condensate

In order to compare our results with the existing experiments on quasi-isotropic condensates, we will use the following physical constants, corresponding to ^{7}Li atoms in a radial trap: $m = 1.16 \times 10^{-26}$ kg, $\tilde{a} = -27.3 a_0$ (with a_0 the Bohr radius) and $\hat{\omega} = (\tilde{\omega}_x\tilde{\omega}_y\tilde{\omega}_z)^{1/3} = 908.41\,\text{s}^{-1}$. These values yield $a = -5.74 \times 10^{-3}$. With these parameters, the mean-field approximation (6) is expected to be very reliable. Note that we ignore the contributions of

non-condensed atoms. They interact with the condensate only through a nearly constant background density term, inducing no significant change in the dynamics of the system [21].

The values of the energy functional $\mathcal{E}$ and the (smallest absolute value) square eigenvalue λ^2 versus particle number $\mathcal{N}$ are shown as solid lines on figure 2 (top and bottom, respectively). The eigenvalues are imaginary on the metastable elliptic lower branch ($\lambda^2 < 0$) and real on the unstable hyperbolic upper branch ($\lambda^2 > 0$). Using (2) on stationary solutions we obtain $d\mathcal{E}/d\mathcal{N} = \mu$. Thus μ is the slope of $\mathcal{E}$ and the lower branches $\mathcal{E}_-$, λ^2_- (respectively upper branches $\mathcal{E}_+$, λ^2_+) are scanned for $\mu > \mu_c$ (respectively $\mu < \mu_c$). The point $\mu = \mu_c$ determines the maximum number of particles $\mathcal{N} = \mathcal{N}_c$ for which stationary solutions exist. We have checked that all the other pairs of eigenvalues are imaginary on both branches (data not shown).

The dashed curves on figure 2 are derived from the Gaussian variational approximation which will be defined in section III C for the general anisotropic case. In the present isotropic case, this approximation can be solved in closed form, yielding the expressions [15]:

$$\mathcal{N}(\mu) = \frac{4\sqrt{2\pi^3}\left(-8\mu + 3\sqrt{7+4\mu^2}\right)}{7|\tilde{a}|\left(-2\mu + \sqrt{7+4\mu^2}\right)^{3/2}}, \qquad (25)$$

$$\mathcal{E} = \mathcal{N}(\mu)\left(-\mu + 3\sqrt{7+4\mu^2}\right)/7. \qquad (26)$$

The number of particles $\mathcal{N}$ is maximal at $\mathcal{N}_c^G = 8\sqrt{2\pi^3}/|5^{5/4}a|$ for $\mu = \mu_c^G = 1/2\sqrt{5}$. The eigenvalues can also be obtained in closed form from the linearized equations of motion [15]:

$$\lambda^2(\mu) = 8\mu^2 - 4\mu\sqrt{7+4\mu^2} + 2 \qquad (27)$$

By inspection of figure 2 it is apparent that both the solution of the GP equation and the Gaussian variational approximation share the same qualitative behavior, with quantitative discrepancies. Figure 3 shows the physical origin of the quantitative errors in the Gaussian approximation. It is apparent that the exact solution is well approximated by a Gaussian only for small $\mathcal{N}$ on the stable (elliptic) branch.

B. Hamiltonian Saddle Node Normal Form

The qualitative behavior displayed on figure 2 by the physical quantities $\mathcal{E}$ and λ^2 near the critical value $\mathcal{N} = \mathcal{N}_c$ is the generic signature of a HSN bifurcation defined, at lowest order, by the normal form [23, 24]

$$\ddot{q} = \delta - \beta q^2, \qquad (28)$$

where $\delta = (1 - \mathcal{N}/\mathcal{N}_c)$ is the bifurcation parameter, β is a dimensionless constant, and q is the coordinate describing the state of the system in the direction of the phase
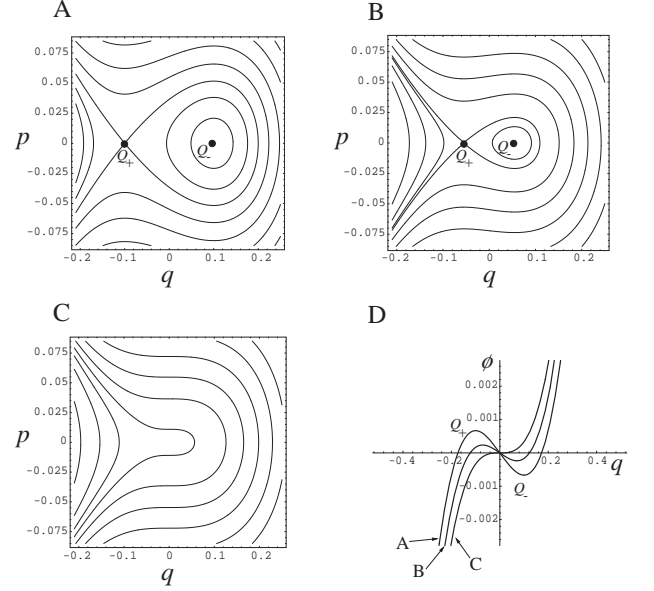

FIG. 4: Phase portraits of the Hamiltonian saddle-node normal form (28), with $p = \dot{q}$. A: $\delta = 0.2$, B: $\delta = 0.1$, C: $\delta = 0$. D: Corresponding potential Φ associated to each phase portrait A, B or C, with $\dot{p} = -\partial\Phi/\partial q$. An elliptic region bounded by the separatrix that starts and ends on the fixed point Q_+ (homoclinic orbit) is present on A and B. Phase portrait C displays the critical merging of fixed points Q_+ and Q_+, and the disappearance of the elliptic region.

space that becomes unstable. Indeed, introducing the additional non-dimensional quantities $\mathcal{E}$ and γ to define the appropriate energy

$$\mathcal{E} = \mathcal{E}_0 + \frac{1}{2}\dot{q}^2 - \delta q + \frac{1}{3}\beta q^3 - \gamma\delta, \qquad (29)$$

it is straightforward to derive from (28) that, close to the critical point $\delta = 0$, the universal scaling laws are given by

$$\mathcal{E}_\pm = \mathcal{E}_c - \mathcal{E}_l\delta \pm \mathcal{E}_\Delta\delta^{3/2}, \qquad (30)$$

$$\lambda^2_\pm = \pm\lambda^2_\Delta\delta^{1/2}, \qquad (31)$$

where $\mathcal{E}_c = \mathcal{E}_0$, $\mathcal{E}_l = \gamma$, $\mathcal{E}_\Delta = 2/3\sqrt{\beta}$ and $\lambda^2_\Delta = 2\sqrt{\beta}$. Note that these relations can be inverted to obtain the parameters in (28) from the critical data. For the Gaussian approximation the critical amplitudes can be computed from equations (25) and (26). One finds

$$\mathcal{E}_c = \frac{4\sqrt{2\pi^3}}{5^{3/4}|a|} \qquad (32)$$

$$\mathcal{E}_\Delta = \frac{64\sqrt{\pi^3}}{5^{9/4}|a|} \qquad (33)$$

$$\lambda^2_\Delta = 4\sqrt{10}. \qquad (34)$$

For the exact solutions, we obtain the critical amplitudes $\mathcal{E}_\Delta = 1340$ and $\lambda^2_\Delta = 14.68$ by performing fits on the nu-

FIG. 5: Stationary solutions of the GP equation versus the particle number $\mathcal{N}$ for a non-isotropic potential case with $\omega_r = \hat{\omega}$ and $\omega_z = \hat{\omega}/5$ (*cigar*). Top: value of the energy functional. Bottom: square of the bifurcating eigenvalue ($\lambda_\pm^2$). Solid lines: exact solution of the GP equation. Dashed lines: Gaussian approximation.
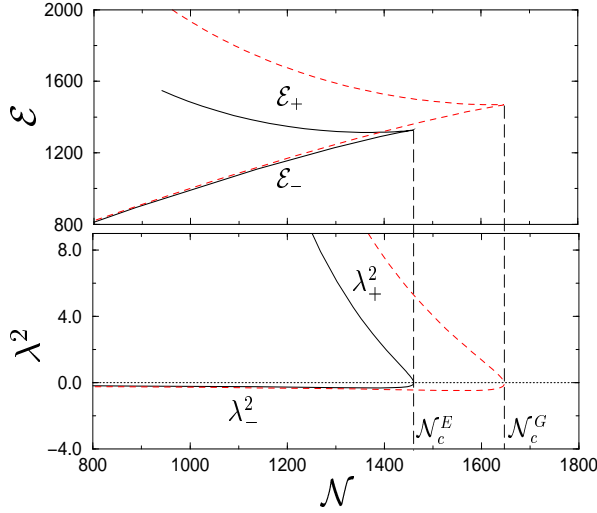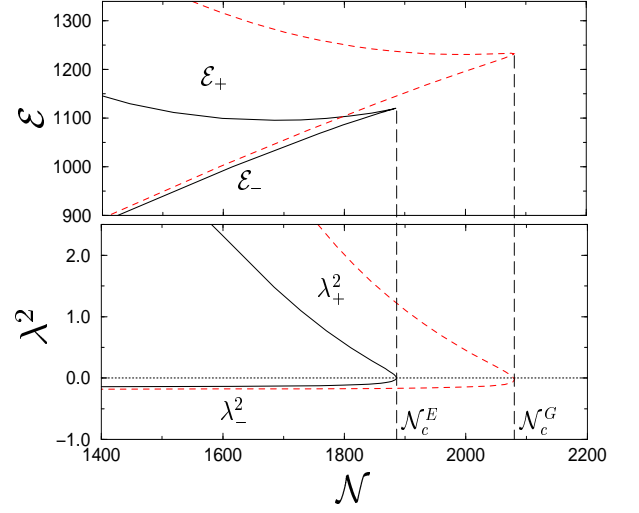

FIG. 6: Stationary solutions of the GP equation versus the particle number $\mathcal{N}$ for a non-isotropic potential case with $\omega_r = \hat{\omega}/5$ and $\omega_z = \hat{\omega}$ (*pancake*). Top: value of the energy functional. Bottom: square of the bifurcating eigenvalue ($\lambda_\pm^2$). Solid lines: exact solution of the GP equation. Dashed lines: Gaussian approximation.

merical data. Comparing both results, we find that the Gaussian approximation captures the bifurcation qualitatively, but with quantitative errors of 17% for $\mathcal{N}_c$ [14], 24% for $\mathcal{E}_\Delta$ and 14% for λ_Δ^2 in the isotropic case [15].

The phase portrait of the normal form is shown on Figure 4. When $\delta = (1 - \mathcal{N}/\mathcal{N}_c) > 0$, equation (28) admits two fixed points $Q_\pm = \mp\sqrt{\delta/\beta}$, as shown in Fig. 4A. Thus, a hyperbolic stationary state and an elliptic stationary state coexist. The phase space is separated into two regions by a separatrix which is a homoclinic orbit linking the hyperbolic stationary state to itself. Trajectories inside the orbit remain bounded near the elliptic fixed point. If the condensate is taken beyond the separatrix by a perturbation (e.g. thermal excitations or quantum tunneling, see below section IV), it will fall into unbounded (hyperbolic) trajectories and collapse. As $\mathcal{N}$ is increased, the hyperbolic and elliptic stationary states approach one another, (Fig. 4B) and the homoclinic orbit inside which orbits are bounded is reduced. The two stationary states join at $\mathcal{N} = \mathcal{N}_c$ (Fig. 4C), at which the HSN occurs. No stationary state exists for $\mathcal{N} > \mathcal{N}_c$.

C. Non-isotropic Condensates

We now briefly present the main expressions obtained from a Gaussian variational analysis of the G-P equation with a cylindrical potential trap. Some of these results have been previously obtained by other authors [17, 18, 30, 31, 32, 33]. We therefore restrict our discussion to the equations that will be used in our analysis of the condensate lifetimes.

The trial function is a Gaussian solution to the linear ($a = 0$) Schrödinger equation in which we incorporate eight variational parameters in order to take into account the anisotropy of the system. The form of the ansatz is given by:

$$\Psi(x, y, z, t) = (A_r(t) + iA_i(t))$$
$$\times \exp\left\{ -\left(\frac{1}{X(t)^2} + i\phi_X(t)\right)\frac{x^2}{2} \right.$$
$$-\left(\frac{1}{Y(t)^2} + i\phi_Y(t)\right)\frac{y^2}{2}$$
$$\left. -\left(\frac{1}{Z(t)^2} + i\phi_Z(t)\right)\frac{z^2}{2} \right\} \quad (35)$$

where the real parameters $\{A_r, A_i\}$, $\{\phi_X, \phi_Y, \phi_Z\}$ and $\{X, Y, Z\}$ are related to the amplitude, the phase and the width of the Gaussian profile respectively. The Euler-Lagrange equations associated with the trial function (35) and the action defined in equation (1) can be reduced to the following system of second-order differential equations:

$$\frac{d^2X}{dt^2} = -\omega_x^2 X - \frac{\nu}{X^2 YZ} + \frac{1}{X^3}$$
$$\frac{d^2Y}{dt^2} = -\omega_y^2 Y - \frac{\nu}{XY^2 Z} + \frac{1}{Y^3}$$
$$\frac{d^2Z}{dt^2} = -\omega_z^2 Z - \frac{\nu}{Z^2 XY} + \frac{1}{Z^3} \quad (36)$$

where

$$\nu = \sqrt{\frac{2}{\pi}}\frac{m\,(\omega_x\omega_y\omega_z)^{1/3}}{\hbar}|\tilde{a}|\mathcal{N}. \quad (37)$$

The evolution of the condensate is better understood by drawing an analogy between its width and the motion of a particle with coordinates (X, Y, Z) moving in the potential

$$U(X, Y, Z) = \frac{1}{2}\left(\omega_x^2 X^2 + \omega_y^2 Y^2 + \omega_z^2 Z^2\right) - \frac{\nu}{XYZ}$$
$$+ \frac{1}{2}\left(\frac{1}{X^2} + \frac{1}{Y^2} + \frac{1}{Z^2}\right). \quad (38)$$

Indeed, defining $P_x = dX/dt$, $P_y = dY/dt$, $P_z = dZ/dt$ and the Hamiltonian

$$H(P_x, P_y, P_z, X, Y, Z) = \frac{1}{2}\left(P_x^2 + P_y^2 + P_z^2\right) + U(X, Y, Z),$$

we find that equations (36) transform into Hamilton's equations of motion.

If we consider now a potential trap (5) with cylindrical symmetry ($\omega_r \equiv \omega_x = \omega_y$) equations (36) can be simplified by using $X(t) = Y(t)$. We thus find that (36) yields two fixed points (X_+, Z_+) and (X_-, Z_-) which describe the stationary solutions for $\Psi(x, y, z, t)$. These obey

$$0 = \omega_r^2 - \frac{4\mu}{7X_\pm^2} - \frac{5}{7X_\pm^4} + \frac{2}{7}\left(\frac{1}{X_\pm^2} + \frac{1}{Z_\pm^2}\right)\frac{1}{X_\pm^2}$$
$$0 = \omega_z^2 - \frac{4\mu}{7Z_\pm^2} - \frac{5}{7Z_\pm^4} + \frac{4}{7}\left(\frac{1}{X_\pm^2 Z_\pm^2}\right), \quad (39)$$

where the chemical potential μ is related to the total number of particles through

$$\mathcal{N} = \frac{2L_0}{7|\tilde{a}|}\sqrt{2\pi}X^2 Z\left(\frac{1}{X^2} + \frac{1}{2Z^2} - \mu\right). \quad (40)$$

The fixed points correspond to a metastable center (X_+, Z_+) and to an unstable saddle point (X_-, Z_-), respectively. They are analogous to the Q_+ and Q_- points appearing in the phase portraits on Figure 4. The solutions to (39) can be computed numerically, together with the linearized variational equations evaluated at every stationary point.

Figures 5 and 6 show $\mathcal{E}$ and λ^2 for the cigar and pancake cases, respectively. The solid lines present the values obtained by discretizing and solving numerically the original differential equations (12) and (22a), using the methods described in the Appendix. The dashed lines were computed using the Gaussian approximation described above. Both the isotropic and non-isotropic cases display saddle-node bifurcations. This is to be expected, since the saddle-node bifurcation is the generic way in which stable and unstable branches meet [23].

It is apparent from figures 2, 5, and 6 that the exact critical number of particles $\mathcal{N}_c^E$ is smaller than the Gaussian value $\mathcal{N}_c^G$ for all three geometries [8, 14, 17, 18]. Table I compares the different critical $\mathcal{N}$ values obtained.

In order to compare properly the HSN bifurcations obtained for the three aspect ratios studied, we can rescale the intensity of the potential to obtain the same $\mathcal{N}_c^E$ for

TABLE I: Critical number of particles obtained for the isotropic, cigar and pancake geometries by using the exact solution of the GP equation ($\mathcal{N}_c^E$) and the Gaussian approximation ($\mathcal{N}_c^G$)

ω_r	ω_z	$\mathcal{N}_c^E$	$\mathcal{N}_c^G$
$\hat{\omega}$	$\hat{\omega}$	1258.5	1467.7
$\hat{\omega}$	$\hat{\omega}/5$	1460.3	1646.6
$\hat{\omega}/5$	$\hat{\omega}$	1885.6	2080.5

TABLE II: Rescaling factors required for having $\mathcal{N}_c = \mathcal{N}_c^{\text{iso}}$ in the cigar and pancake cases. Columns $\mathcal{E}_\Delta$ and λ_Δ^2 show critical amplitudes at the bifurcation for the rescaled $\mathcal{E}$ and λ^2 curves respectively.

ω_r	ω_z	rescaling factor	$\mathcal{E}_\Delta$	λ_Δ^2
$\hat{\omega}$	$\hat{\omega}$		1340	14.68
$c_{\text{cig}}\hat{\omega}$	$c_{\text{cig}}\hat{\omega}/5$	$c_{\text{cig}} = 1.3463$	1000	4.00
$c_{\text{pan}}\hat{\omega}/5$	$c_{\text{pan}}\hat{\omega}$	$c_{\text{pan}} = 2.2447$	550	1.05

all cases. In general, any confining harmonic potential with frequencies ω_r and ω_z that produces a critical number of particles $\mathcal{N}_c$ can be rescaled by a factor

$$c = \left(\frac{\mathcal{N}_c}{\mathcal{N}_c^*}\right)^2, \quad (41)$$

to obtain the a new potential with frequencies $\omega_r^* = c\,\omega_r$ and $\omega_z^* = c\,\omega_z$, which will have the critical number of particles $\mathcal{N}_c^*$. The remaining physical quantities for the new potential are obtained through the following transformations:

$$\Psi^* = \frac{\Psi}{c^{1/4}} \quad (42)$$

$$\mathcal{N}^* = \frac{\mathcal{N}}{\sqrt{c}} \quad (43)$$

$$\mathcal{E}^* = \frac{\mathcal{E}}{\sqrt{c}} \quad (44)$$

$$\lambda^* = \lambda. \quad (45)$$

We choose arbitrarily to rescale the potential intensity so that all $\mathcal{N}_c^E$ are equal to that for the isotropic case $\mathcal{N}_c^{\text{iso}}$. Table II shows the value of the rescaling factors c_{cig} and c_{pan} for the cigar and pancake cases respectively, as obtained from equation (41) using $\mathcal{N}_c^* = \mathcal{N}_c^{\text{iso}}$. The last two columns of this table show the critical amplitudes obtained for the rescaled $\mathcal{E}$ and λ^2 curves. These were obtained by fitting the HSN asymptotic forms given in relations (30) and (31) to the rescaled data.

IV. LIFETIME OF CONDENSATES

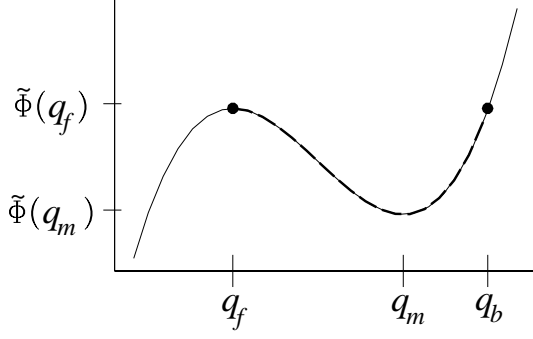In this section we first find expressions for the TIC, MQT and ICO decay rates. Using the numerical data

FIG. 7: Bounce trajectory (dashed) over the Euclidean potential $\tilde{\Phi}(q)$. Points q_f, q_m and q_b indicate the fixed point, the minimum of $\tilde{\Phi}(q)$ and the bounce point, respectively.

presented in the previous section, we then compute these decay rates for the $\omega_r = \omega_z$ (isotropic), $\omega_r/5 = \omega_z$ (cigar) and $\omega_r = \omega_z/5$ (pancake) cases. Finally, we compare the results obtained for these three potential geometries by studying the spontaneous isotropization of the condensates.

A. Definition and Computations of Decay Rates

The TIC (thermally induced collapse) decay rate Γ_T is estimated using the formula [25]

$$\frac{\Gamma_T}{\hat{\omega}} = \frac{|\lambda_+|}{2\pi} \exp\left[\frac{-\hbar\hat{\omega}}{k_B T}\left(\mathcal{E}_+ - \mathcal{E}_-\right)\right] \quad (46)$$

where $\hbar\hat{\omega}(\mathcal{E}_+ - \mathcal{E}_-)$ is the (dimensionalized) height of the nucleation energy barrier (with $\hat{\omega}$ the reference frequency introduced in Section II A), T is the temperature of the condensate and k_B is the Boltzmann constant. Note that the prefactor characterizes the typical decay time which is controlled by the slowest part of the nucleation dynamics: the top-of-the-barrier saddle point eigenvalue λ_+ and not λ_- as used in [9]. However, near the bifurcation both eigenvalues scale in the same way and the behavior of Γ_T can be obtained directly from the universal saddle-node scaling laws (30) and (31). Thus the exponential factor and the prefactor vanish respectively as $\delta^{3/2}$ and $\delta^{1/4}$.

We estimate the MQT (macroscopic quantum tunneling) decay rate using an instanton technique that takes into account the semi classical trajectory giving the dominant contribution to the quantum action path integral [8, 9]. We approximate this so-called bounce trajectory by the solution of the equation of motion

$$\frac{d^2 q(t)}{dt^2} = \frac{-d\tilde{\Phi}(q)}{dq} \quad (47)$$

starting and ending at the fixed point q_f of the phase space where $\mathcal{E}(q_f) = \mathcal{E}_-$. The Euclidean potential $\tilde{\Phi}(q)$

is defined so that $-\tilde{\Phi}(q)$ reconstructs the Hamiltonian dynamics in the region scanned by the bounce trajectory (see Figure 7). We represent it by a fourth-order polynomial of the form

$$\tilde{\Phi}(q) = \alpha_0 + \alpha_2 q^2 + \alpha_3 q^3 + \alpha_4 q^4 \quad (48)$$

coefficients α_0, α_2, α_3 and α_4 chosen such that

$$\tilde{\Phi}(0) = -\mathcal{E}_+ \quad (49a)$$
$$\tilde{\Phi}(q_f) = -\mathcal{E}_- \quad (49b)$$
$$\partial_q^2 \tilde{\Phi}(0) = -\lambda_+(\mathcal{N}) \quad (49c)$$
$$\partial_q^2 \tilde{\Phi}(q_f) = -\lambda_-(\mathcal{N}) \quad (49d)$$

We thus obtain a semi-analytic polynomial expression for $\tilde{\Phi}(q)$ where the coefficients are determined through the numerical values presented in figures 2, 5, and 6.

Once $\tilde{\Phi}(q)$ and the bounce point q_b (defined through the relation $\tilde{\Phi}(q_b) = \tilde{\Phi}(q_f)$) are known, the MQT rate is estimated as

$$\frac{\Gamma_Q}{\hat{\omega}} = \sqrt{\frac{|\lambda_-|v_0^2}{4\pi}} \exp\left[\frac{-4}{\sqrt{2}} \int_{q_f}^{q_b} \sqrt{\tilde{\Phi}(q) - \tilde{\Phi}(q_f)}\,dq\right], \quad (50)$$

where v_0 is defined by the asymptotic form of the bounce trajectory $q(t)$ as it approaches q_f [9], given by $q(\tau) \sim q_f + (v_0/|\lambda_-|)\exp[-|\lambda_-\tau|]$.

In the same way as was done for the TIC, universal scaling laws can be derived close to criticality from (28), (30) and (31). We find that the exponential factor in (50) follows the same scaling as $\sqrt{|\mathcal{E}_+ - \mathcal{E}_-|}\,dq$. It therefore vanishes as $\sqrt{\delta^{3/2}}\delta^{1/2} = \delta^{5/4}$. The asymptotic form of $q(t)$ shows that dq follows the same law as $v_0/|\lambda_-|$. Thus $v_0 \sim \delta^{3/4}$, and the prefactor vanishes as $\sqrt{\delta^{1/4}}\delta^{3/4} = \delta^{7/8}$. Note that these universal scaling laws agree with those already derived in the Gaussian case in [8].

The TIC (46) and MQT (50) decay rates obtained for the exact and Gaussian stationary states are shown in Figure 8. To validate these results we checked that the Gaussian TIC decay rates computed in [13] are found when we (incorrectly at a finite distance from criticality) replace λ_+ by λ_- in equation (46) (data not shown). We also checked that our Gaussian MQT decay rate agrees with the one previously computed in [8].

The ICO (inelastic two and three body collision) atomic decay rates are evaluated using the formula $d\mathcal{N}/dt = f_C(\mathcal{N})$ with

$$f_C(\mathcal{N}) = K \int |\Psi|^4 d^3\mathbf{x} + L \int |\Psi|^6 d^3\mathbf{x}, \quad (51)$$

where $K = 3.8 \times 10^{-4}[s^{-1}]$ and $L = 2.6 \times 10^{-7}[s^{-1}]$ as in [10, 11]. In order to compare the particle decay rate (51) to the condensate collective decay rates obtained for the TIC and MQT, we compute the condensate ICO half-life using

$$\tau_{1/2}(\mathcal{N}) = \int_{\mathcal{N}/2}^{\mathcal{N}} \frac{dn}{f_C(n)} \quad (52)$$
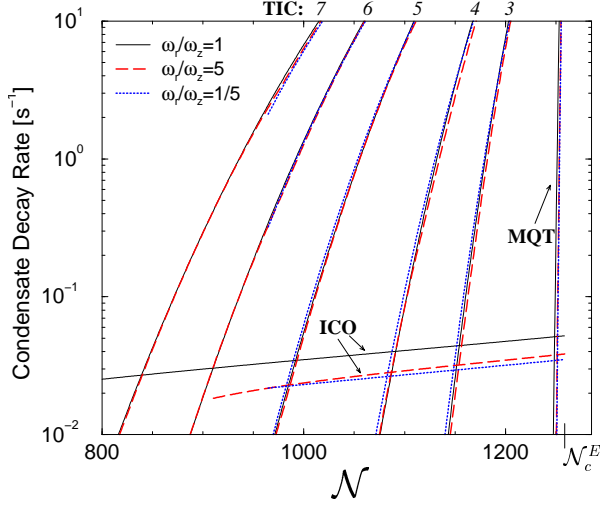
FIG. 8: Condensate decay rates versus particle number for the isotropic potential $\omega_r = \omega_z = \hat{\omega}$ (solid), and for the rescaled cigar potential $\omega_r = c_{\mathrm{cig}}\hat{\omega}$, $\omega_z = c_{\mathrm{cig}}\hat{\omega}/5$ (dashed) and pancake potential $\omega_r = c_{\mathrm{pan}}\hat{\omega}/5$, $\omega_z = c_{\mathrm{pan}}\hat{\omega}$ (dotted). ICO: inelastic collisions. MQT: macroscopic quantum tunneling. TIC: thermally induced collapse at temperatures 50 nK (3), 100 nK (4), 200 nK (5), 300 nK (6), and 400 nK (7).
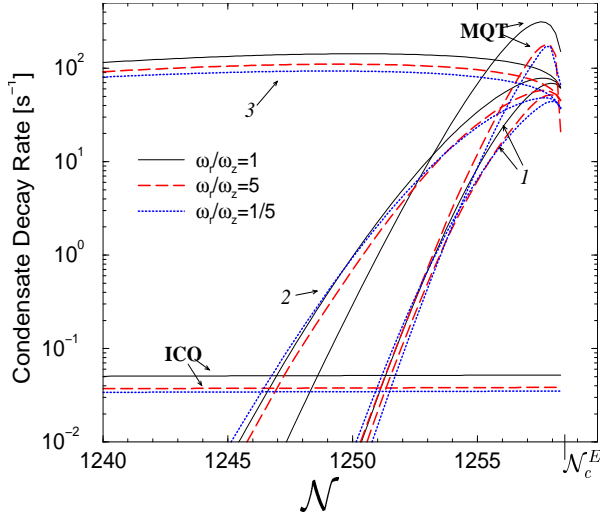

FIG. 9: Enlargement of the crossover region between the quantum tunneling and the thermal decay rate. ICO: inelastic collisions. MQT: macroscopic quantum tunneling. TIC: thermally induced collapse at temperatures 1 nK (1), 2 nK (2) and 50 nK (3).

and plot $\tau_{1/2}^{-1}$ on figure 8.

Figures 8 and 9 compare the condensate decay rates for the isotropic and the cigar and pancake potentials, rescaled by c_{cig} and c_{pan} as described in Section III C. We note that the three aspect ratios generate very similar results after rescaling. The relative magnitudes of the different decay rates – TIC, MQT, and ICO – are the
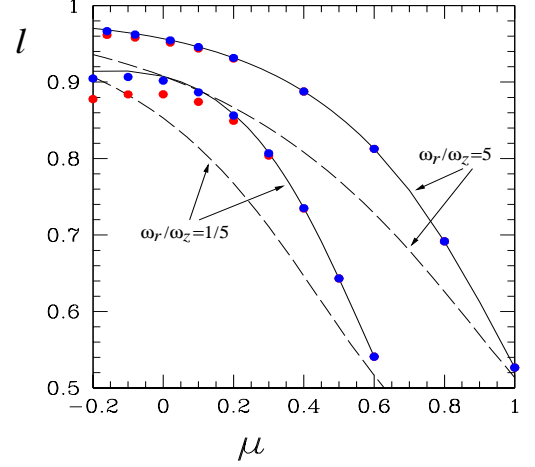

FIG. 10: Ellipticity ratio ℓ as a function of μ. Solid curves show numerical results, dashed curves the Gaussian approximation. For the cigar, $\ell \equiv \ell_r/\ell_z$ (upper curves) and for the pancake, $\ell \equiv \ell_z/\ell_r$ (lower curves). Dots show results obtained by using successively fewer Fourier modes in the numerical results; dots nearer to (further from) each curve correspond to retaining 7/8 (6/8) of the Fourier modes. ℓ changes by less than 1% for $\mu > -0.8$ ($\mu > -0.2$) for the cigar (pancake) case and by less than 0.1% at the saddle-node bifurcation at $\mu = 0.38$ ($\mu = 0.31$) for the cigar (pancake) case.

same for the three cases. At $T \leq 1[\mathrm{nK}]$ the MQT effect becomes important compared to the ICO decay in a region very close to $\mathcal{N}_c^E$ ($\delta \leq 8 \times 10^{-3}$). This was shown in [8] using Gaussian computations but evaluating them with the exact maximal number of condensed particles $\mathcal{N}_c^E$. Figure 9 shows that even for temperatures as low as 2[nK], the TIC decay rate exceeds the MQT rate except in a region extremely close to $\mathcal{N}_c$ ($\delta < 5 \times 10^{-3}$), where the condensates will live less than $10^{-1}[s]$. Thus, in the experimental case of $^7\mathrm{Li}$ atoms, the relevant effects are ICO and TIC, with the crossover that is shown on Figure 9.

B. Spontaneous Isotropization of Condensates

The decay rates of the isotropic and non-isotropic cases shown in figure 8 are quite similar, despite the fact that ω_z and ω_r differ by a factor of five. We have investigated this question by examining the wave functions Ψ for the pancake and cigar cases. These wave functions are peaked at the origin, as shown on figure 3. Their characteristic length scales in the axial and radial directions, ℓ_z and ℓ_r, can be measured by computing the ratios of the value of Ψ to its curvature at the origin.
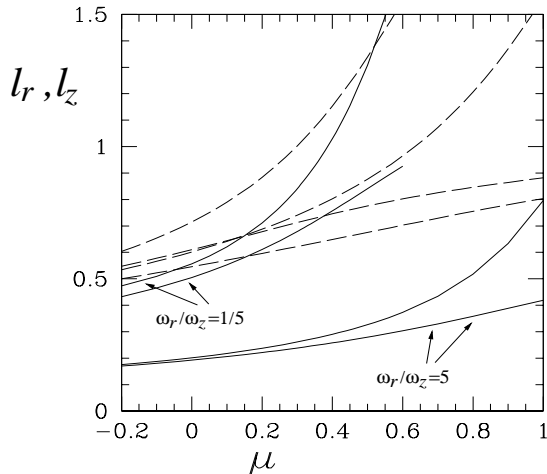
FIG. 11: Length scales ℓ_r, ℓ_z as a function of μ. Solid curves show numerical results, dashed curves the Gaussian approximation. Cigar case shown in lower curves (with $\ell_r < \ell_z$), pancake in upper curves (with $\ell_z < \ell_r$). The size of the condensate decreases drastically as μ decreases, i.e. away from the saddle-node bifurcation along the unstable branch.

More specifically, we define

$$\ell_z^2 \equiv \Psi \left(\frac{\partial^2 \Psi}{\partial z^2} \right)^{-1} \quad (r = 0, z = 0) \tag{53a}$$

$$\ell_r^2 \equiv \Psi \left(\frac{1}{r} \frac{\partial}{\partial r} r \frac{\partial \Psi}{\partial r} \right)^{-1} \quad (r = 0, z = 0) \tag{53b}$$

We then obtain the ellipticity of the wavefunction as the ratio ℓ of these length scales: $\ell = \ell_r/\ell_z$ for the cigar and $\ell = \ell_z/\ell_r$ for the pancake. These ellipticity ratios are shown in figure 10 as a function of μ. For large μ, i.e. away from the saddle-node bifurcation along the stable branch, ℓ decreases rapidly away from one, indicating that the wave function is highly non-isotropic. At the saddle-node bifurcation, $\ell = 0.89$ at $\mu = 0.38$ for the cigar and $\ell = 0.80$ at $\mu = 0.31$ for the pancake. As μ is decreased, i.e. as we leave the saddle-node bifurcation along the unstable branch, ℓ approaches one as the wave function becomes more nearly spherically symmetric. This trend is present both in the numerical solution to the G-P equation and in the Gaussian approximation, as can be seen on figure 10. Since the decay rates result from the scaling behavior near the saddle-node bifurcation, where the condensate is fairly isotropic, it follows that the decay rates are similar for the cigar, pancake, and spherically symmetric geometries, as we have shown on Figures 8 and 9.

The spontaneous isotropization of condensates when μ is decreased can be understood by the following phenomenological reasoning. When $-\mu$ grows, the balance of terms in the right hand side of equation (6) changes. For small $-\mu$, it is dominated by the the isotropic ∇^2 and

the anisotropic $V(x)$ terms. But for large $-\mu$, the wavefunction Ψ is strongly peaked and the ∇^2 and nonlinear terms, both isotropic, become dominant.

Figure 10 also provides a test of our numerical spatial resolution. By computing the ellipticity ℓ for different Fourier truncation levels, we show that ℓ changes with the resolution for low μ, especially for the pancake case, where we used fewer Fourier modes than in the other calculations. Note however that our decay rate calculations only use results near the saddle-node bifurcation, where ℓ varies by less than 0.1% when different truncation levels are used. This indicates that Ψ was adequately resolved in the region of interest.

As μ is decreased, the wave functions become more highly peaked for both our numerical results and for the Gaussian approximation (see figures 3 and 11). This is the main reason for the declining accuracy. To continue the computations further, the size of the periodic box should be reduced along with μ. We believe that, with adequate resolution, all of the exact wave functions would become spherically symmetric as μ decreases, as do the Gaussian approximations.

V. CONCLUSION

We have demonstrated that it is possible to numerically compute the stationary states, the bifurcating eigenvalues and the lifetime of anisotropic attractive Bose Einstein condensates.

The Gaussian mean field approximation was found to have significant quantitative errors for all the different confining potential geometries that were studied, when compared with numerical solutions to the G-P equation.

Spontaneous isotropization of the metastable condensate was found to occur as the critical number of particles is approached, yielding a life-time that depends weakly on the anisotropy of the confining potential.

Direct methods – Gaussian elimination and diagonalization – were used in treating the spherically symmetric case, of size 128, but are far too costly for the three-dimensional case, of size 10^6. In fact, since we only calculated axisymmetric stationary states and eigenvectors with an additional midplane symmetry, an intermediate two-dimensional axisymmetric cylindrical representation could have been implemented, of size 5000, permitting the use of direct methods. Our purpose, however, has been to construct and explore numerical methods appropriate for a general non-isotropic case.

The methods used to compute stationary states and bifurcating eigenvalues for the non-isotropic cases where essentially analogous. Each consists of a powerful and rapid outer iteration: Newton's method for the stationary states and the inverse Arnoldi method for the eigenvalues. The large linear systems that need to be inverted within each method are solved by the same inner biconjugate gradient iteration – BiCGSTAB – and constitutes the main numerical difficulty. Its convergence is greatly

improved by an inverse Laplacian preconditioning which is empirically tuned by adjusting the pseudo-timestep σ in Newton's method or the shift s in Arnoldi's method.

Our results and implementation have demonstrated that all these numerical techniques can be successfully combined to calculate the stationary states and eigenvectors for the G-P equation in a confining potential with an arbitrary three-dimensional geometry.

APPENDIX: NUMERICAL METHODS

1. Spatial Discretization

The operators L and W defined in (10) and (11) are spatially discretized using the pseudospectral method [26]. For the isotropic case, the spherically symmetric $\Psi(r,t)$ is expanded as a series of even Chebyshev polynomials $T_{2n}(r/R)$, on which the boundary condition $\Psi(R,t) = 0$ is imposed. The domain is taken to be $0 \leq r \leq R = 4$ and the resolution used is $N_R = 128$. For the non-isotropic cases, we use a three-dimensional periodic Cartesian domain and Ψ is expanded as a three-dimensional trigonometric (Fourier) series. The cigar case is solved in a periodic domain of size $(L_x, L_y, L_z) = (5.39, 5.39, 12.04)$ in units of L_0, using $(N_x, N_y, N_z) = (96, 96, 96)$ gridpoints or trigonometric modes (with a 2/3 dealiasing rule,) so the total number of gridpoints or trigonometric functions is as high as $N_{3D} = 10^6$. (The more poorly resolved pancake case was calculated using $(L_x, L_y, L_z) = (12.04, 12.04, 5.39)$ and $(N_x, N_y, N_z) = (48, 48, 96)$.) The harmonic potential (5) is approximated by a periodic potential by writing $x = \arcsin(\sin(x))$ and Taylor-expanding the arcsin function. This leads to a Fourier series for the potential, which is truncated according to the resolution used.

Pseudospectral methods require performing over Ψ, at every iteration, a Chebyshev transform in the isotropic case or a Fourier transform in the non-isotropic case. These operations consume a time proportional to $N_R \log N_R$ or $N_{3D} \log(N_{3D})$, respectively. Actions and inversions of the Laplacian L are carried out on the Chebyshev or Fourier representations of Ψ, while actions of the multiplicative operator W are carried out on its grid representations. The time required by these operations scales approximately linearly in N_R or N_{3D}.

2. Stationary States

As stated in section II B, the stationary states of (6) that correspond to minima of $\mathcal{E}$ at a given value of $\mathcal{N}$ can be obtained by integrating to relaxation the diffusion equation

$$\frac{\partial \Psi}{\partial t} = L\Psi + W(\Psi) \tag{A.1}$$

where the initial data $\Psi(t = 0)$ has a total number of particles $\mathcal{N}$ and the value of the Lagrange multiplier μ is fixed during the relaxation by the condition $\partial \mathcal{N}/\partial t = 0$.

To integrate (A.1) a mixed implicit-explicit first-order time-stepping scheme is used:

$$\Psi(t + \sigma) = (I - \sigma L)^{-1}(I + \sigma W)\Psi(t) \tag{A.2}$$

where I is the identity operator. The Helmholtz operator $(I - \sigma L)^{-1}$ is easily inverted in the Chebyshev or Fourier representation. The motivation for integrating L implicitly is to avoid the extremely small timesteps that would otherwise be necessitated by the wide range of eigenvalues of the Laplacian.

This relaxation method is equivalent to that used in [14] and can only reach the stable stationary solutions of (A.1). In order to also capture unstable stationary solutions [27] we implemented a Newton branch-following algorithm [15, 28]. We search for fixed points of (A.2), a condition strictly equivalent to the stationarity of (6):

$$\begin{aligned} 0 = B\Psi(t) &\equiv \Psi(t + \sigma) - \Psi(t) \\ &= (I - \sigma L)^{-1}(I + \sigma W)\Psi(t) - \Psi(t) \\ &= \left[(I - \sigma L)^{-1}(I + \sigma W) - I\right]\Psi(t) \\ &= (I - \sigma L)^{-1}\left[(I + \sigma W) - (I - \sigma L)\right]\Psi(t) \\ &= (I - \sigma L)^{-1}\left[(\sigma(L + W)\right]\Psi(t). \end{aligned} \tag{A.3}$$

Solutions to (A.3) are found using Newton's method. We begin with an initial estimate Ψ, in our case the solution at a neighboring value of μ. Newton's method calls for approximating the nonlinear operator B whose roots are sought by its linearization B_Ψ about Ψ. We seek a decrement ψ such that $\Psi - \psi$ solves this linearized equation:

$$\begin{aligned} 0 &= B(\Psi - \psi) \approx B(\Psi) - B_\Psi \psi \\ B_\Psi \psi &= B(\Psi). \end{aligned} \tag{A.4}$$

Ψ is then replaced by $\Psi - \psi$ and equation (A.4) solved again for a further decrement. The process is iterated until $B(\Psi)$ or ψ is sufficiently small. In our case, equation (A.4) takes the form

$$(I - \sigma L)^{-1}\sigma(L + DW)\psi = (I - \sigma L)^{-1}\sigma(L + W)\Psi. \tag{A.5}$$

We will explain how we solve the large linear problem (A.5) in section 3.

The role of σ is formally that of the timestep in (A.2), but in (A.5), its value can be taken to be arbitrarily large. For $\sigma \to \infty$, (A.5) becomes:

$$L^{-1}(L + DW)\psi = L^{-1}(L + W)\Psi. \tag{A.6}$$

For the spherically symmetric case, the linear system (A.6) is of size $N_R = 128$ and can be solved by standard Gaussian elimination. The boundary condition $\psi(r = R) = 0$ is imposed by modifying the operator L^{-1} or $(I - \sigma L)^{-1}$, as it is in the time-stepping algorithm (A.2).

To compute the full branch of solutions as a function of μ, we begin from a stable state of (A.1) at a small value of $\mathcal{N}$ obtained by time-integration. Each stationary state is computed in $3 - 5$ Newton iterations.

3. Conjugate Gradient Solution of Linear Systems

For the periodic Cartesian case, the linear system (A.6) of size $N_{3D} = 10^6$ is too large to be stored or inverted directly: the operation count for Gaussian elimination would be of the order of N_{3D}^3. Instead, we use BiCGSTAB [29], a variant of the well-known conjugate gradient method, developed for linear systems which are not symmetric definite. Such methods are matrix-free, meaning that they require only the right-hand-side of (A.6), and a subroutine which acts with the linear operator of the left-hand-side. A solution to the linear system is constructed as a carefully chosen linear combination of powers of the linear operator acting on the right-hand-side.

For a periodic Cartesian geometry, conjugate gradient methods are particularly economical, since operator actions are all accomplished in a time proportional to N_{3D}. However, conjugate gradient methods for nonsymmetric definite systems may converge slowly (requiring a large number of evaluations of the linear operator) or even not at all. This happens when the operator is poorly conditioned, i.e. roughly when it has a wide range of eigenvalues. One must then precondition the linear system, i.e. multiply both sides of the system by a matrix which improves its conditioning and accelerates convergence. Since for operators such as $L + DW$, the wide range of eigenvalues is due primarily to those of L, we expect L^{-1} to be an effective preconditioner. From (A.5), it can be seen that σ allows us to interpolate between linear operators $\sigma(L+DW)$ and $L^{-1}(L+DW)$. We vary σ empirically to optimize the convergence of BiCGSTAB. A few hundred BiCGSTAB iterations are usually required to solve the linear system.

A further advantage of iterative inversion methods is that they can produce a (non-unique) solution even when the linear operator is singular. This is the case for our operators, which have the neutral modes described in section II C, as well as other neutral modes related to symmetries and the Fourier representation. The preconditioner, however, is inverted exactly. If (A.6) is used, the constant Fourier mode is treated separately which allows us to construct an invertible version of the singular operator L.

4. Eigenvalue Problem

We now describe our numerical method for calculating the linear stability of the stationary states. For the spherically symmetric case, the eigenvalues of (17) are computed by constructing and diagonalizing the corresponding matrix for each converged stationary solution. The results reported were generated with a Mathematica code running on a workstation. With the values $R = 4$, $N_R = 128$, the first two eigenvalues of the harmonic oscillator are obtained with a precision better than 0.05%.

For the three-dimensional case, it is again not possible to construct and diagonalize the matrix of size $N_{3D} = 10^6$ directly: the operation count for diagonalization is also of the order N_{3D}^3. Instead, we calculate only eigenvalues of interest, using a variant of the iterative inverse power method. The inverse power method calculates the eigenvalues of a matrix M closest to a value s by means of the sequence defined by:

$$(M - sI)\psi_{j+1} = \psi_j \qquad (A.7)$$

The sequence $\{\psi_j\}$ converges rapidly to the eigenvector whose eigenvalue is nearest to s, with the eigenvalue λ of M estimated by $(\lambda - s)^{-1} \approx \langle \psi_{j+1}, \psi_j \rangle / \langle \psi_j, \psi_j \rangle$.

In order to calculate complex or multiple eigenvalues, and to obtain more precise eigenvalues and error estimates, we use the sequence generated by (A.7) to implement the more general Arnoldi or Krylov method [34]. Instead of retaining only the last two members of the sequence, the last K members (typically 4 or 6) are orthonormalized and then assembled into the $K \times K$ matrix $H_{jk} \equiv \langle \psi_j, (M - sI)^{-1}\psi_k \rangle$. The eigenvalues of H provide estimates of up to K of the eigenvalues $(\lambda - s)^{-1}$ of $(M - sI)^{-1}$.

In our implementation of the Arnoldi method for (22a), we seek the eigenvalues λ^2 of the matrix $-(L+DW^I)(L+DW^R)$. Rather than solving (A.7), we solve the equivalent preconditioned problem [28]

$$L^{-2}[-(L+DW^I)(L+DW^R) - sI]\psi_{j+1} = L^{-2}\psi_j \quad (A.8)$$

by using BiCGSTAB. From (A.8) we obtain a sequence of vectors containing an increasing proportion of the desired eigenvectors, but since our solution of (A.8) is not exact, we then construct H by multiplication rather than inversion via $H_{jk} \equiv \langle \psi_j, M\psi_k \rangle$. We can then estimate the eigenvalues λ^2 by those of H. Although the formal role of s is that of a shift which focuses the inverse iteration on the eigenvalues being sought, here we also use it empirically to improve the convergence of BiCGSTAB.

The inverse Arnoldi method requires between 3 and 10 iterations to converge, each of which requires several hundred BiCGSTAB iterations in order to solve its associated linear system.

[1] C. C. Bradley, C. A. Sackett, J. J. Tollett, and R. G. Hulet, Phys. Rev. Lett. **75**, 1687 (1995).

[2] C. C. Bradley, C. A. Sackett, and R. G. Hulet, Phys. Rev. Lett. **78**, 985 (1997).

[3] J. L. Roberts, N. R. Claussen, S. L. Cornish, E. A. Donley, E. A. Cornell and C. E. Wieman, Phys. Rev. Lett. **86**, 4211 (2001).

[4] K. Strecker, G. Partridge, A. Truscott, and R. Hulet, Nature **417**, 150 (2002).

[5] F. Schreck, L. Khaykovich, K. L. Corwin, G. Ferrari, T. Bourdel, J. Cubizolles and C. Salomon, Phys. Rev. Lett. **87**, 080403 (2001).

[6] F. Schreck, G. Ferrari, K. L. Corwin, J. Cubizolles, L. Khaykovich, M.-O. Mewes and C. Salomon, Phys. Rev. A **64**, 011402 (2001).

[7] A. Görlitz, J. M. Vogels, A. E. Leanhardt, C. Raman, T. L. Gustavson, J. R. Abo-Shaeer, A. P. Chikkatur, S. Gupta, S. Inouye, T. Rosenband and W. Ketterle, Phys. Rev. Lett. **87**, 130402 (2001).

[8] M. Ueda and A. J. Leggett, Phys. Rev. Lett. **80**, 1576 (1998).

[9] H. T. C. Stoof, J. Stat. Phys. **87**, 1353 (1997).

[10] H. Shi and W.-M. Zheng, Phys. Rev. A **55**, 2930 (1997).

[11] R. J. Dodd, M. Edwards, C. J. Williams, C. W. Clark, M. J. Holland P. A. Ruprecht and K. Burnett, Phys. Rev. A **54**, 661 (1996).

[12] Y. Kagan, G. V. Shlyapnikov, and J. T. M. Walraven., Phys. Rev. Lett. **76**, 2670 (1996).

[13] C. A. Sackett, H. T. C. Stoof, and R. G. Hulet., Phys. Rev. Lett. **80**, 2031 (1998).

[14] P. A. Ruprecht, M. J. Holland, K. Burnett, and M. Edwards, Phys. Rev. A **51**, 4704 (1995).

[15] C. Huepe, S. Métens, G. Dewel, P. Borckmans and M. E. Brachet, Phys. Rev. Lett. **82**, 1617 (1999).

[16] A. Gammal, T. Frederico and L. Tomio, Phys. Rev. E **60** 2421 (1999)

[17] A. Gammal, L. Tomio, and T. Frederico, Phys. Rev. A

[18] A. Gammal, T. Frederico, and L. Tomio, Phys. Rev. A **64**, 055602 (2001).

[19] E. P. Gross, Nuovo Cimento **20**, 454 (1961).

[20] L. P. Pitaevskii, Sov. Phys. JETP **13**, 451 (1961).

[21] M. Houbiers and H. T. C. Stoof, Phys. Rev. A **54**, 5055 (1996).

[22] Wen-Chin Wu and A. Griffin, Phys. Rev. A **54**, 4204 (1996).

[23] J. Guckenheimer and P. Holmes, *Nonlinear Oscillations, Dynamical Systems and Bifurcations of Vector Fields* (Springer-Verlag, Berlin, 1983).

[24] C. Elphick, E. Tirapegui, M. E. Brachet, P. Coullet and G. Iooss, Physica D **29**, 95 (1987).

[25] C. Gardiner, *Handbook of Stochastic Methods* (Springer-Verlag, Berlin, 1985).

[26] D. Gottlieb and S. A. Orszag, *Numerical Analysis of Spectral Methods* (SIAM, Philadelphia, 1977).

[27] R. Seydel, *From Equilibrium to Chaos: Practical Bifurcation and Stability Analysis* (Elsevier, New York, 1988).

[28] L.S. Tuckerman & D. Barkley, *Bifurcation analysis for time-steppers*, in Numerical Methods for Bifurcation Problems and Large-Scale Dynamical Systems, ed. by E. Doedel & L.S. Tuckerman (Springer, New York, 2000), p. 452–466.

[29] H. van der Vorst, SIAM J. Sci. Stat. Comput. **13**, 631 (1992).

[30] V. M. Pérez-Garcia, H. Michinel, J. I. Cirac, M. Lewenstein and P. Zoller, Phys. Rev. A **56**, 1424 (1997).

[31] V. M. Pérez-Garcia, H. Michinel, and H. Herrero, Phys. Rev. A **57**, 3837 (1998).

[32] F. K. Abdullaev, A. Gammel, L.Tomio, and T. Frederico, Phys. Rev. A bf 63, 043604 (2001).

[33] S. K. Adhikari, Phys. Rev. E **65**, 016703 (2002).

[34] W. E. Arnoldi, Q. Appl. Math. **9**, 17 (1951).